Taylor & Francis
Taylor & Francis Group

REVIEWS

Nonlinear effects in fiber lasers and amplifiers: review of pulse generation at 1550–1870 nm wavelength range
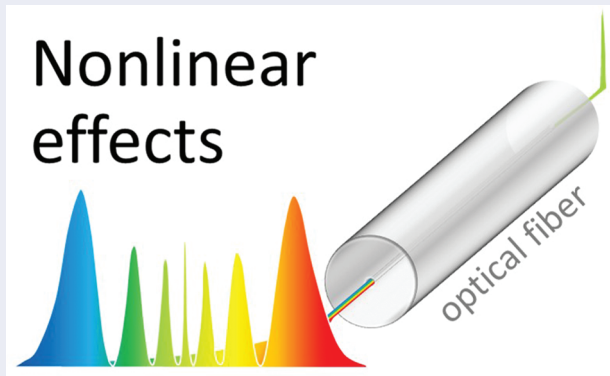
Diana Galiakhmetova (ID)

Aston Institute of Photonic Technologies, Aston University, Birmingham, UK

ABSTRACT

Fiber lasers, operating in the NIR-III spectral region (1550–1870 nm), have attracted the attention of scientists due to their widespread applications and potential advancement of biomedical tools and clinical laser-based systems. However, developing tunable NIR-III ultrashort pulsed lasers is still challenging due to the lack of efficient rare-earth-doped fibers, reviewed in this paper. Overcoming these challenges and achieving wide tunability are possible by implementing methods based on nonlinear optical effects. This review presents recent advances in developing NIR-III fiber lasers, including the explanation of nonlinear effects such as self-phase modulation, four-wave mixing, stimulated Raman scattering, soliton self-frequency shift, and supercontinuum generation. In addition, the paper discusses the advantages and drawbacks of each method and makes recommendations for future development trends and improvements.

GRAPHICAL ABSTRACT

CONTACT Diana Galiakhmetova ✉ d.galiakhmetova@aston.ac.uk 🖭 Aston Institute of Photonic Technologies, Aston University, Aston Triangle, Birmingham, West Midlands B4 7ET, UK

1. Introduction

Recently, laser systems operating within the 1550–1870 nm wavelength range have garnered remarkable interest in development due to their significance in biomedicine, material processing, gas detection, and other applications. This high attention occurs because of the unique spectral properties of this wavelength range.

In biomedicine, this spectral region is called the third near-infrared (NIR-III) tissue transparency or biological window with increased tissue penetration depth. It is characterised by low light scattering and absorption by water, haemoglobin, melanin, and other proteins [1–3]. The NIR-III laser systems are promising tools for biological imaging [4,5], coherent anti-Stokes and stimulated Raman spectroscopy [6,7], optical coherent microscopy and tomography [8], endoscopy [9], and surgery [10].

However, the advancement of NIR-III lasers faces significant challenges due to the limited number of viable gain mechanism options operating in this wavelength region. The most accessible laser types are semiconductor, fiber, and solid-state lasers.

The quantum-well semiconductor lasers based on AlGaInAs/InP and InGaAsP/InP materials can emit light within the wavelength range of 1250–2100 nm [11,12]. Nevertheless, the manufacturing process of supercontinuum lasers is challenging, and they exhibit drawbacks such as limited thermal conduction properties of quaternary AlGaInAs and sensitivity to environmental factors like humidity, temperature, and vibrations [13].

Fiber laser development faces challenges in identifying a suitable gain medium operating efficiently in this wavelength range and achieving pulse generation and amplification with the required output parameters. We will discuss pulsed fiber lasers operating in the NIR-III range due to the only emission effects of active fibers in Section 2.1.

The development of solid-state NIR-III lasers is achievable exclusively by exploiting nonlinear optical effects in crystals [14–18].

1.1. Nonlinear effects

The majority of NIR-III laser sources involve nonlinear optical effects arising from the interaction of high-intensity light with nonlinear media such as molecules, polymers, or crystals. The nonlinear response is related to the anharmonic oscillation of the material's bound electrons under the influence of the applied field [19,20]. In the electric field $E(t)$, the polarisation $P(t)$ induced by the electric dipole is not linear [21]:

$$P = \varepsilon_0 \left[\chi^{(1)} E + \chi^{(2)} E^2 + \chi^{(3)} E^3 + ... \right] \tag{1}$$

where ε_0 is the vacuum permittivity, while $\chi^{(1)}$, $\chi^{(2)}$, and $\chi^{(3)}$ are linear, second-order, and third-order nonlinear susceptibilities of the medium, respectively.

1.2. Second-order nonlinear effects

Second harmonic, sum and difference frequency, and parametric generation are examples of second-order nonlinear effects that play a crucial role in generating light at new wavelengths [22]. Optical parametric amplifiers (OPAs) and oscillators (OPOs) are commonly used techniques to generate pulses in the NIR-III region. They are based on the interaction of three distinct waves: pump (ω_p), signal (ω_s), and idler (ω_i) that should satisfy conditions of energy conservation ($\hbar\omega_p = \hbar\omega_s + \hbar\omega_i$) and phase-matching ($\Delta k = k_p - k_s - k_i = 0$), where k_p, k_s, and k_i are the k vectors corresponding to the frequencies ω_p, ω_s, and ω_i [23,24].

OPAs amplify low-intensity signal waves from pump laser sources in crystals with high parametric nonlinearity (Figure 1a). For example, Y.W. Tzeng et al. [25] demonstrated an ultra-short OPA system with a wideband of 700–1900 nm, an average power of 140 mW, and a repetition rate of 50 MHz. The developed OPA was based on a supercontinuum (SC) fiber laser and a 1 cm long multi-channel periodically poled lithium niobate (PPLN) crystal. However, the generated white noise from the SC source adversely affects the quality of bioimaging [26].

Another technique that allows to avoid the SC laser as a pump source and reduce the noise level is OPO [15–17,26–28]. In the case of OPO, a nonlinear medium is located in the laser cavity, and the signal is created due to pump wave and cavity feedback (Figure 1b). For example, M.V. O'Connor et al. [27] developed a 330-fs synchronously pumped PPLN-based oscillator operating in the wavelength range of 1550–1950 nm with an average output power of about 90 mW. In this setup, an ultrashort-pulse Ytterbium-doped fiber (YDF) laser with an average power of 410 mW was used as a pump source.

The main advantages of OPO and OPA are wide wavelength tunability and high power spectral density [14,29,30], which are required in bioimaging,
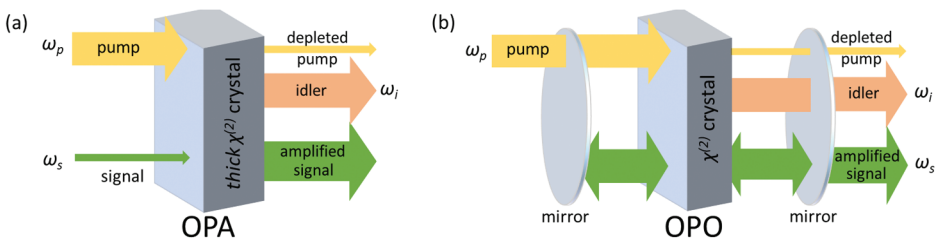

Figure 1. Schematic of (a) optical parametric amplifier and (b) oscillator.

time-resolved spectroscopy, chemical sensing, and microscopy. Neverthe-less, these systems are characterised by increased sensitivity to white noise from seed sources and external environmental factors such as temperature fluctuations and mechanical vibrations. Since OPO and OPA setups include free-space optical elements, they require careful stabilisation and precise alignment, complicating system design, and operation. Moreover, their bulk-iness and significant physical space represent considerable disadvantages for their use as portable devices for biomedical purposes.

1.3. Third-order nonlinear effects

For materials with inversion symmetry, such as optical fibers, $\chi^{(2)}$ disappears, and usual optical fibers do not exhibit second-order nonlinear effects [31]. The lowest-order nonlinear effects originate from the third-order suscepti-bility $\chi^{(3)}$, which is responsible for four-wave mixing (FWM) and nonlinear refraction phenomena (will be discussed in Section 2.2).

Compared to crystal-based laser systems, all-fiber lasers demonstrate ad-vantages in compact size, resistance to fluctuations in temperature and hu-midity conditions, and comparatively cost-effective production. However, the availability of lasers operating in this wavelength range is limited due to nu-merous obstacles encountered in developing a compact NIR-III pulsed laser system at each design stage: master oscillator, amplifier, and wavelength shift.

This paper demonstrates the recent achievements in developing NIR-III fiber lasers, including the review of possible gain mediums, nonlinear effect-based methods of pulse generation, and their pros and cons.

2. Fiber laser systems

2.1. Emission effects of active fibers

Certain active fibers, including Bismuth-doped (BDF), Erbium-doped (EDF), Thulium-doped (TDF), and Thulium/Holmium co-doped (THDF) fibers, find application in fiber lasers and amplifiers that operate in restricted regions within the NIR-III spectrum. Table 1 shows the input and output parameters of NIR-III pulsed fiber lasers and amplifiers utilising population inversion (PI) in BDF and rare-earth-doped fibers (Table 1, PI).

2.1.1. Bismuth-doped fiber
In contrast to rare-earth-doped fibers, BDFs exhibit the remarkable capabil-ity to emit continuous-wave light across a wide wavelength range in NIR-III, spanning from 1650 nm to 1800 nm [111–115]. However, the development of all-fiber lasers operating in pulsed mode presents challenges.

A notable breakthrough in this domain occurred when T. Noronen et al. [32] demonstrated a laser based on a 5 m long BDF and a carbon nanotube

Table 1. NIR-III pulsed fiber lasers and amplifiers: gain mechanism (GM), doped-fiber (DF) and its length l, nonlinear fiber (NF), output parameters (operation wavelength λ_{out}, average power P_{av}, pulse duration τ, repetition rate R_r, maximum pulse energy E_p), input parameters to DF/NF (pump wavelength λ_p, average power $P_{av,p}$, threshold power $P_{av,p\,thld}$), the complexity of the system (all-fiber (all-f), includes customised fiber (CF), or free space elements (FSEs)), and demonstrated application.

GM	DF,l (m)	NF,l (m)	λ_{out} (nm)	P_{av} (mW)	τ (fs)	R_r (MHz)	Max. E_p (nJ)	Pump	λ_p (nm)	$P_{av,p}$ (W)	$P_{av,p\,thld}$ (mW)	Com.	App.	Ref., year
PI	BDF, 5		1713–1733	10	1200–14000	44–600	1.7	EDFL	1565	1.2	300	All-F, CNTs		[32] 2016
PI	EDF, 9		1562	2–8	8–23×10^9	0.02–0.04	150	LD	980	0.309	62	All-F		[33] 2024
PI	EDF, 5		1587–1592	50	700	6.95	3	RFL	1480	3.2	400	All-F, GSA		[34] 2009
PI	EDF, 0.165		1559–1565	1.94	682	1028	0.002	LD	976	~0.335	~222	All-F, CNTs		[35] 2024
PI	THDF, 0.5		1705–1805	2.3–12	630–930	232.6–554.6	0.02	EDFL	1556	2.7	700–2300	FSEs, AOTF		[36] 2016
PI	TDF, 0.8 + 1.3 + 1.5		1782–1788	690	445	46.4	14	EDFL	1560	2.6	380 (?)	FSEs		[37] 2017
PI	TDF, 2–2.5		1702–1764, 1788–1831	?	2520–3310	3.2–14.3	?	CW Ti:Sa	788	0.18 + 0.1 + 0.26	?	All-F		[38] 2017
PI	TDF, 2		1750–1810	?	2320	3.2	?	CW Ti:Sa	788	0.18	?	All-F		[39] 2015
PI	TDF, 3.2		1737–1754	3.55	230–370	17.84	0.2	EDFL+ EDFA	1560	1.3	1040	FSEs		[40] 2021
PI	TDF, 0.75 + 0.6 + 0.15		1700–1900	140	478–18×10^3	17	8.2	2×EDFL +EDFA	1550	2.2 + 2.7	200	FSEs		[41] 2023
PI	TDF, 0.16–0.18		1700, 1725, 1750	750	17×10^6	0.01	75300	EDFL+ EDFA	1560	3	700	All-F	PA	[42] 2020
PI	TDF, 0.8		1720–1800	126–264	294–507	22.7	11.6	EDFL+ EDFA	1550	3	584	FSEs		[43] 2024
SPM	PM EDF, 0.6		1546–1586	?	142	52	?	LD	976	0.25	63	All-F		[46] 2023
SPM		ND-HNLF, 5.8	1492–1664	51	~56	182	0.28	EDFL	1550	0.78	?	FSEs	OCT	[47] 2016
SPM		ND-HNLF, ?	1510–1890	48.3	122	47.96	1	EDFL	1560	?	?	All-F	OCM	[48] 2016 [49] 2012

(Continued)

Table 1. (Continued).

GM	DF/ (m)	NF/ (m)	Output parameters					Input parameters				Com.	App.	Ref., year
			λ_{out} (nm)	P_{av} (mW)	τ (fs)	R_r (MHz)	Max. E_p (nJ)	Pump	λ_p (nm)	P_{avp} (W)	$P_{avp\ thld}$ (mW)			
SPM		HNLF, 0.02	1300–1700	140–220	97–182	31	7.1	EDFL+ EDFA+ EYDFA	1550	1.74	500	FSEs		[50] 2017
SPM		DCF38, 0.04	1350–1700	230–330	52–143	31	10.6	EDFL+ EDFA+ EYDFA	1550	3	650	FSEs		[50] 2017
SPM	W-type ND TDF, 1.5 + 5		1740–1892	180	2760	5.5	32.7	EDFL+ EDFA, CW EDFL	1565,1565	2,2	?	All-F, SESAM		[51] 2020
SPM	W-type ND TDF, 1.6 + 5		1775–1795	1016	174	7.82	128.0	EDFL+ EDFA, CW EDFL	1565,1565	1.98,4.4	1250,820	All-F		[52] 2021
FWM		DSF, 40	1320–1395, 1720–1820	<1	7000–17×10³	10	0.018	EDFL+ EDFA, CW EDFL	1532–1549	0.03 (?)	?	All-F		[53] 2010
FWM		HNL-DSF, 50	1413–1543, 1573–1695	0.6–4.5	8000–10000	156.2 (?)	0.03 (?)	EDFL+ ED-FAs	1544–1559	0.02–0.1	20	All-F		[54] 2009
FWM		DSF, 7–15	1319–1518, 1617–1876	~15	14–35×10³	7.2	2	EDFL	1546–1568	0.1	~50	All-F		[55] 2018 [56] 2018
FWM	EDF, 2.59	PM, 5.51	1567–1608	19	151	16.3	1.16	LD	980	0.9, 0.7	332, 200	All-F		[57] 2021
FWM	EYDF, 2	HNLF, 0.05 PM DSF, 3.5	1684–1716	1420	450	~34	40	EDFL+ EDFA	1557–1565	6.5	?	All-F, CNTs		[58] 2020 [59] 2020

(Continued)

Table 1. (Continued).

GM	DF,l (m)	NF,l (m)	λ_out (nm)	P_av (mW)	Output parameters τ (fs)	R_r (MHz)	Max. E_p (nJ)	Pump	Input parameters λ_p (nm)	P_avp (W)	P_avp,thld (mW)	Com.	App.	Ref., year
FWM	TDF, 1.5	HNLF, 50	1815–1968	200–400	2×10^6	~3.2	125	EDFL, EDFL	1546–1562,1570	0.5,2	520,200	All-F		[60] 2016
SRS		PM Raman F, 26.8	1652–1665	27	300	6.54	3.6	EDFL, EDFL, EDFA	1550	0.05	5	All-F		[61] 2023
SRS		HC-PCF, 20	1687–1723	820	0.2×10^6	0.5	1600	EDFL+ ED- FAs	1527–1567	1.4	250	FSEs, Gas cell		[62] 2020
SRS		HC-PCF, 10–20	1693–1705	3300	$12\text{-}15\times10^6$	1.3–2	1600	EDFL+ EDFA	1540–1550	7.5	1000	FSEs, Gas cell		[63] 2020 [64] 2020
SRS		HC-PCF, 9	1693–1705	1630	10×10^6	1	1600	EDFL+ EDFA	1550	6	1000	FSEs, Gas cell		[65] 2021
SRS		HC-PCF, 50	1693, 1801	1500	30×10^6	6	250	EDFL+ EDFA	1540	6	3600	FSEs, Gas cell		[66] 2021
SRS		Raman F, ?	1630–1765	23000	1×10^{11}	0.002	11.5×10^6	YDFL	1117	280	15000	All-F		[67] 2020
SRS	EDF, ?	PM Raman F, 50	1490–1610	~17	150	6.7	3.7	LD	976	?	?	All-F		[68] 2021
SRS	PM EDF, 2.5		1510–1645	6.9	$60\times10^3\text{-}0.2\times10^6$	0.1–5	1.1	LD	1480	0.27	120	All-F		[69] 2012
SRS	TDF, 2.7	SMF, 2000-8000	1699	2500	?	?	?	EYDFL	1565	11.6–21.5	7300	All-F		[70] 2022

(Continued)

Table 1. (Continued).

GM	DF,l (m)	NF,l (m)	λ_{out} (nm)	P_{av} (mW)	Output parameters			Pump	λ_p (nm)	Input parameters		Com.	App.	Ref., year
					τ (fs)	R_r (MHz)	Max. E_p (nJ)			$P_{av,p}$ (W)	$P_{av,p\,thld}$ (mW)			
SRS	GDF, 5		1703–1729	22.62	4300	24.8	1	EDFL+ EDFA	1612	0.177	83.68	All-F		[71] 2022
SRS	GDF, 10000	HNLF, 100	1666–1667	5	2000	1.72	3	CW EDFL	1555	15 + 6	9500	All-F, CNTs		[72] 2011
SSFS		SMF-28, 2500	1555–1830	?	300–2000	~20.2	?	EDFL	1555	0.003	0.2	All-F		[73] 2007
SSFS		PMF, 75	1560–1780	8.5	203	48 (?)	0.2 (?)	EDFL	1556	0.01	3	FSEs		[74] 1999
SSFS		HNLF, ?	1700–2100	19.8	72–107	45	0.44	EDFL+ EDFA	1560	0.115	39	All-F		[75] 2017
SSFS		PM-HN-DSF, 0.07	1130–1950	15	24–40	67	0.2	EDFL+ EDFA	1550	0.11	?	FSEs		[76] 2004
SSFS		PM-HN-DSF, 100	1560–2030	20 (?)	103–330	~50	0.52	EDFL	1556	0.025	3	FSEs		[77] 2001
SSFS		HNL-DSF, 23–580	1560–1720	150	110–240	10×10^3 (?)	0.015 (?)	EDFL+ EDFA	1549–1555	0.3–1.3	300	All-F, EAM		[78] 2003
SSFS		TASMF, 0.15	1300–1650	80 (?)	62–85	80	1	Ti:Sa+ OPO	1300	0.02–0.2	20	FSEs, CF		[79] 2001
SSFS		HN PCF, 10	1050–1690	2.6–30	100–150	41.3	0.7	YDFL	1050	0.075	~10 (?)	FSEs		[80] 2006
SSFS		LMA35, 1.1	1580 – 2130	1–44.8	70	1	44.8	EDFL	1550	0.02–0.28	20	All-F	THG	[81] 2011 [82] 2014
SSFS		LMA25, 46	1560–1700	87–277	192–200	1–10	2.8	EDFL+ EDFA	1544	1	?	FSEs		[83] 2011
SSFS		LMA PCF, 3.5	1600	125–550	80–95	42	13	EDFL+ EDFA	1560	0.44–1.25	440	FSEs		[84] 2013
SSFS		LMA PCF, 1	1780 – 1600–1700	114	83–166	10.9	10.4	EDFL+ EYDFA	1550	1	172	FSEs		[85] 2022

(Continued)

Table 1. (Continued).

GM	$DF_l/$ (m)	$NF_l/$ (m)	λ_{out} (nm)	P_{av} (mW)	Output parameters τ (fs)	R_r (MHz)	Max. E_p (nJ)	Pump	λ_p (nm)	Input parameters $P_{av,p}$ (W)	$P_{av,p\,thld}$ (mW)	Com.	App.	Ref., year
SSFS		DSF, 5.9–7.7	1700–1740	26.8	196	38.8	0.7	EDFL	1550	0.035	13	All-F		[86] 2017
SSFS		ARBF, 1.45	1680, 1800	95	85	1	95	EDFL+ EDFA	1560	~1	326	FSEs, CF	3PEF	[87] 2021
SSFS		PM PC, 0.36	1660–1715	22	65–100	~1	67	EDFL	1550	~0.5	?	FSEs, PC rod	3PEF	[88] 2013
SSFS		Raman F, 960	1610–1850	6.8	800	7.719	0.88	EDFL+ EDFA+ EYDFA	1560	0.12	9.1	All-F		[89] 2017
SSFS	EDF, 0.45	PMF, 460	1696–1703	35	384	102	0.34	LD	976	0.37–1.4	1020	All-F		[90] 2019
SSFS	LMA EDF, 3	LMA Raman F, 2	1650–1700	400	70–75	50	9	EDFL, LD	1565,976	0.01,20	?	All-F	3PEF	[91] 2017
SSFS	ED PM VLMA, 3	PM VLMA, 15	1620–1990	1600	108–120	80	18	EDFL, RFL	1530,1480	0.08,50	80,3800	All-F, CF	TREF	[92] 2019
SSFS	ED PM VLMA, 3		1560–1672	~2000	86	100	21	EDFL, RFL	1530,1480	0.1,20	100,6000	All-F, CF		[93] 2016
SSFS	EYDF, 2.6		1600–1700	717	91.2–133	86.7	8.2	EDFL, LD	1573,976	0.2,12	200,7000	All-F	MPM	[94] 2023
SC		SMF-28, 4.6	1300–2500	2000	~1×10^6 (?)	0.2	1×10^4 (?)	DFB LD+ EDFA	1550	10	2500	All-F		[95] 2012
SC		HNLF, 1000	1590–1960	~170	60×10^3–1.8×10^5	170–2000	0.85	EDFL+ EDFA	1550–1560	2	800	All-F, AWG		[96] 2018 [97] 2020

(Continued)

Table 1. (Continued).

GM	DF,l (m)	NF,l (m)	Output parameters					Pump	Input parameters			Com.	App.	Ref., year
			λ_{out} (nm)	P_{av} (mW)	τ (fs)	R_r (MHz)	Max. E_p (nJ)		λ_p (nm)	$P_{av,p}$ (W)	$P_{av,p,thld}$ (mW)			
SC	EDF, 6.6	HNLF, 20–140	1330–2030	25	10×10^6	0.739	33	LD	1480	1.7	808	All-F		[98] 2020
SC		PMF, ? HNLF, ?	1579–1821	60	~140	110	0.54	EDFL, EDFA	1560	0.2	?	FSEs	OCT	[99] 2014
SC		PMF, ? ND-HNLF, ?	1521–1879	30	~120	~48	0.63	EDFL, EDFA	1560	?	?	FSEs	OCT	[100] 2011
SC		HNL-PCF, 4.6	1600–2180	1000	0.1×10^6	75	13	EDFL+ EDFA+ EYDFA	1561–1567	2.7	~100	All-F, CNTs		[101] 2016
SC	EDF, 8	PM-HN-DSF, 0.2–5	980–2570	215	41.3	116	1.9	EDFL, LD	1560,1480	0.008, 2×0.4	?	All-F		[102] 2005
SC	YDF, 0.6 + DC EDF, 1	HNLF, 0.045	1040–1750	5700	135	35	160	EDFL+ EDFA, LD	1550,976	0.04, 22.5	?	All-F, CNTs	SRS	[103] 2010
SC	DC YDF, 5		1064–2000	7×10^4–1.8×10^5	$\sim1\times10^6$	0.282	0.43×10^6	YDFL+ YDFA, LD	1060–1068, 976	9.87, 6×50	?	All-F		[7] 2014 [104] 2012
SC	DC YDF, 3		1064–1700	7×10^4	$\sim1\times10^6$	0.282	0.2×10^6	YDFL+ YDFA, LD	1058–1070, 976	4.65,2×50	4650,15000	All-F		[105] 2012
SC	LMA YDF, 25		690–2350	7.1×10^5	3×10^4–1.5×10^5	0.8–2	0.36×10^6	YDFL+ YDFA, LD	1065976	102,2×800	10×10^4, 25×10^4	All-F		[106] 2023
SC	DC YDF, 2.2	SM-2000, 145	856–2141	160	$\sim3\times10^6$	0.003–0.005	3.2×10^4	LD	976	3	1400	All-F		[107] 2024
SC	DC EYDF, 3	SM-2000, 150	1600–2160	465	4.5×10^5	0.015	3.1×10^4	LD	976	4.9	1100	All-F		[108] 2023
SC	BEDF, 0.49	PCF, 100	1250–1910	?	131	42	?	LD	1480	1	?	All-F		[109] 2012
SC	UHNA7, 20		1700–2300	86.4	977	21.1	4.4	TDFL+ TDFA	1915	0.286	38	All-F, CNTs		[110] 2019

(a)

1560 nm
pump

CNT

1560/1730   19 m SMF 5 m BDF
WDM

Coupler   Loop
             Mirror

35% output

(b)

5% output

PDI

PC   PC

WDM   WDM

2.5 m TDF

788 nm pump   788 nm pump

0.3 m PCF
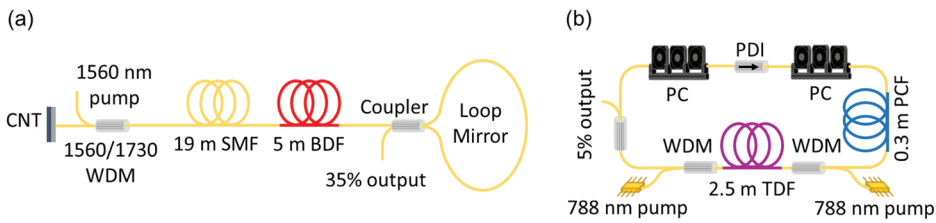
Figure 2. Schematic representation of (a) 14 ps Bismuth-doped fiber (BDF) laser with a carbon nanotube (CNT) saturable absorber, operating at a wavelength range of 1713–1733 nm; (b) ~3 ps tunable fiber laser based on thulium-doped fiber (TDF) and photonic-crystal fiber (PCF) as a wavelength-selective filter. The operation wavelength of 1702–1764 nm and 1788–1831 nm depends on PCF's specifications. (WDM – wavelength-division multiplexing; SMF- single-mode fiber; PC – polarisation controller; PDI – polarisation-dependent isolator). Adapted from [32] and [38] under terms of the CC-BY licence.

(CNT) saturable absorber to achieve a mode-locking regime. It resulted in the generation of 14 ps (1.2 ps after compression) pulses at a pulse repetition rate of 44–600 MHz within the wavelength range of 1713–1733 nm (Figure 2a).

2.1.2. Erbium-doped fiber

Compared to BDFLs, EDFLs exhibit higher repetition rates and pulse energies due to the improved doping properties of the fibers. This advantage stems from the fact that EDFLs require fewer meters of doped fiber, resulting in a shorter laser cavity length.

However, despite a large number of published works on developed fiber lasers and amplifiers with D-shape or tapered EDFs, various co-dopants or implemented saturable absorbers such as semiconductor saturable absorber mirrors (SESAMs), phosphorene, graphene (GSA), CNTs or other inorganic nanostructures, the operating wavelength of pulsed EDFLs has a right-side spectrum limit of around 1620 nm.

2.1.3. Thulium/Holmium co-doped fiber

Recently, T. Noronen et al. [36] demonstrated a 630 fs tunable THDFL operating at a spectral region of 1705–1805 nm with a repletion rate of about 232.6–554.6 MHz. As a pump source, they used an EDFL operating at a wavelength of 1556 nm. The experimental setup was a ring cavity laser with a 50 cm long THDF, an isolator, and an acousto-optic tunable filter (AOTF). The last one was necessary to filter the generated signal and shift frequency. The tunable laser produced stable harmonic mode-locked pulses with a peak power of 21 pJ at a wavelength of 1735 nm (Table 1, PI, THDF).

2.1.4. Thulium-doped fiber

Pure TDFs, devoid of any Holmium additives, can also be used effectively as the active fibers in NIR-III laser setups. Fabricating these fibers is a less intricate process, eliminating the need for complex manufacturing techniques to

ensure the proper integration of Thulium and Holmium ions into the fiber core and decrease the challenges associated with maintaining the desired performance characteristics.

S. Emami et al. [38] successfully showcased the functionality of a TDFL laser operating on the edge of the third tissue transparency window. TDFL exhibited remarkable performance characteristics, generating 3.3 ps pulses across a wavelength span of 1850–1920 nm with a repetition rate of 14 MHz. The incorporation of photonic crystal fibers (PCFs) as wavelength-selective filters enabled pulse generation within the spectral ranges of 1702–1764 nm and 1788–1831 nm, depending on PCFs' inner hole and outer ring diameters (2.5/1.1 μm and 1.9/0.7 μm, respectively). The schematic diagram of the experimental setup is shown in Figure 2b.

Recently, C. Li et al. [42] demonstrated a TDFL applicable to photoacoustic (PA) imaging. In this work, they used a TDF of only 16–18 cm in length. This laser setup generated pulses with a width of approximately 17 ns, a repetition rate of 10 kHz and provided energy output ranging between 60 and 75 μJ for operations in 1700 nm, 1725 nm, and 1750 nm wavelengths.

In recent years, significant progress has been made in developing fiber lasers based on the emission effect of active fibers. Breakthroughs have been made through innovations in mixing dopants and increasing the dopant concentration in fibers, enabling them to emit light effectively within the NIR-III spectral range.

Nevertheless, the lack of materials for an active gain medium with robust gain characteristics in this spectral region poses several obstacles to achieving pulse generation in a wide spectral range. There are still limits regarding the tunability and conversion efficiency of rare-earth doped fiber lasers that restrict their application.

2.2. Third-order nonlinear effects

An approach to overcome obstacles of rare-earth-doped fiber lasers requires the involvement of optical nonlinear effects in the laser system. In the right conditions, nonlinear effects allow the shift of the operating wavelength of rare earth materials from their emission peaks to the region of the NIR-III spectral region. Nonlinear effects, including self-phase modulation (SPM), four-wave mixing (FWM), stimulated Raman scattering (SRS), soliton self-frequency shift (SSFS), and SC generation, introduce complex changes in duration, frequency, and phase during pulse propagation through nonlinear fibers [116]. These phenomena can lead to an increase in output power and enhance laser efficiency.
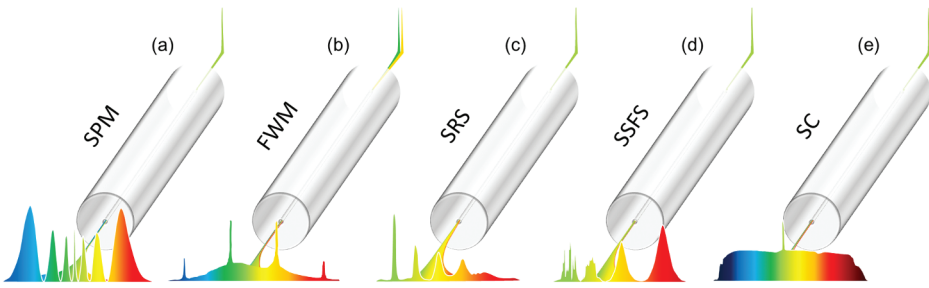
Figure 3. Schematic representation of typical optical spectra of (a) SPM, (b) FWM, (c) SRS, (d) SSFS, and (e) SC.

The operating wavelength of pulsed fiber lasers based on TDF, EDF, YDF, Germanium-doped (GDF), Bismuth/Erbium co-doped fiber (BEDF), Erbium/Ytterbium co-doped fiber (EYDF), and nonlinear effects appearing in various fibers with a third-order nonlinearity $\chi^{(3)}$ are represented in Table 1 in sections SPM, FWM, SRS, SSFS, and SC. Figure 3 shows typical optical spectra of (a) SPM, (b) FWM, (c) SRS, (d) SSFS, and (e) SC.

2.2.1. SPM

In $\chi^{(3)}$ (Kerr) medium like silica-based fibers, when the light intensity is high enough, the response of the medium to the electric field becomes nonlinear, and the refractive index is no longer constant but varies depending on the optical intensity. This dependency, known as the optical Kerr effect, is responsible for multiple phenomena, including FWM and cross-phase modulation in fibers [117].

When short pulses (10 ps-1 ns) propagate through standard single-mode fiber (SMF), which length is significantly shorter than the dispersion length (« 5 km at 1100–1550 nm), the dispersion term can be neglected, estimating that the pulse maintains its shape. In that scenario, only linear losses and the nonlinear term induced by the Kerr effect influence the pulse propagating through the fiber [31]. In that condition, the change in refractive index due to the Kerr effect as light propagates through the fiber will cause a nonlinear phase shift in the pulse and induce a chirp [118]. This chirp grows in magnitude as the pulse travels over a longer distance of fiber, involving the continuous generation of new frequencies on both sides, ultimately broadening the pulse spectrum (Figure 3a).

In 2017, A. Khegai et al. [44,45] successfully demonstrated the first ps-pulsed BDFL using the nonlinear Kerr effect to broaden the laser spectrum. The laser configuration adopted a figure-eight all-fiber design with a non-linear amplifying loop mirror (NALM), generating sub-21 ps pulses. The pulses had a repetition rate of ~4 MHz and an energy level exceeding 80 pJ. Through further amplification with 100 m BDF, the signal experienced power
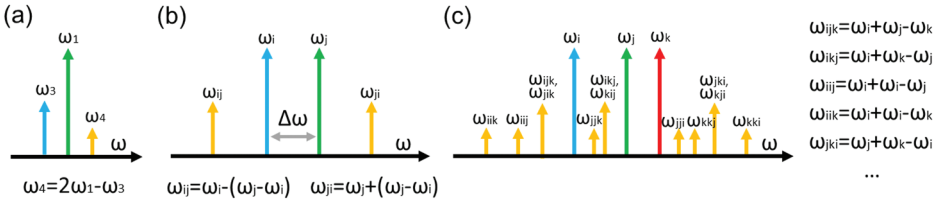
Figure 4. FWM schemes for (a) degenerate case: high-intensity pump wave with frequency ω_1 (green arrow), amplified signal (ω_3 (blue arrow)) and generated idler (ω_4 (yellow arrow)); (b) partially degenerate case: generation of two new waves with frequencies ω_{ij} and ω_{ji} (yellow arrows) from incident components (ω_i (blue arrow) and ω_j (green arrow)); (b) non-degenerate case: creation of new frequencies (yellow arrows) from three incident waves with frequencies ω_i, ω_j, and ω_k (blue, green, and red arrows, respectively).

amplification and SPM due to the high nonlinearity of the BDF and high peak power. That resulted in the spectral broadening from 1702–1706 nm to 1696–1712 nm and increasing of pulse energy to ~ 6 nJ (Table 1, SPM, BDF). Despite the ability to shorten pulses to 630 fs, BDFLs are limited to an average power of tens of milliwatts [112], resulting in relatively low pulse energy that is insufficient for bioimaging.

2.2.2. FWM

Another nonlinear process caused by the Kerr effect in optical fibers is FWM. This nonlinear optical effect is characterised by four waves interacting with each other due to the third-order nonlinearity of the material [119].

In the case of optical fibers, if two of the four frequencies coincide ($\omega_1=\omega_2$), the process is usually called degenerate FWM [120,121]. One of the examples is a high-intensity pump wave with an angular frequency (ω_1) that provides an amplification of a neighbored frequency component, signal (ω_3) (Figure 4a).

For each photon added to the signal wave, two photons are taken away from the pump wave, and one is put into an idler wave with a frequency ω_4, which is:

$$\omega_4 = 2\omega_1 - \omega_3. \tag{2}$$

In addition that the angular frequency detuning is governed by the law of energy conservation, it is crucial to meet the phase-matching condition [31]:

$$k = \Delta k_M + \Delta k_W + \Delta k_{NL} = 0, \tag{3}$$

where Δk_M, Δk_W, Δk_{NL} represent the mismatch occurring due to material dispersion, waveguide dispersion, and the nonlinear effects, respectively.

For the degenerate FWM:

$$\Delta k_M = \tilde{\beta}_3 + \tilde{\beta}_4 - 2\tilde{\beta}_1 \tag{4}$$

$$\Delta k_{NL} = 2\gamma P_1, \tag{5}$$

where $\tilde{\beta}_j(\omega) = n_j\omega_j/c$ is the propagation constant of the wave at the frequency ω_j, while c is the speed of light in a vacuum, n_j is a material index, γ is fiber nonlinear coefficient, and P_j is incident pump power.

Since each component $\tilde{\beta}_j$ from Eq 4 can be expanded into the Taylor series centred at the pump's angular frequency (ω_1), including up to the fourth-order terms, Δk_M can be determined as:

$$\Delta k_M \approx (\omega_3 - \omega_1)\beta_1 + \frac{1}{2}(\omega_3 - \omega_1)^2\beta_2 + \frac{1}{6}(\omega_3 - \omega_1)^3\beta_3 + \frac{1}{24}(\omega_3 - \omega_1)^4\beta_4$$
$$+ (\omega_4 - \omega_1)\beta_1 + \frac{1}{2}(\omega_4 - \omega_1)^2\beta_2 + \frac{1}{6}(\omega_4 - \omega_1)^3\beta_3 + \frac{1}{24}(\omega_4 - \omega_1)^4\beta_4 \tag{6}$$

where β_1, β_2, β_3, β_4 are 1st, 2nd, 3rd and 4th - order dispersion parameters at the pump frequency ω_1. Using the definition of the frequency shift Ω_s [31]:

$$\Omega_s = \omega_1 - \omega_3 = \omega_4 - \omega_1 \tag{7}$$

Eq 6 can be simplified to:

$$\Delta k_M \approx \Omega_s^2\beta_2 + \frac{1}{12}\Omega_s^4\beta_4. \tag{8}$$

In SMF, $\Delta k_W \approx 0$ because changes in the material indices are nearly identical for all waves. If the pump wavelength ($\lambda_1 = 2\pi c/\omega_1$) is not too close to the fiber zero-dispersion wavelength (λ_0), then $\Delta k_M \approx \Omega_s^2\beta_2$. For SMF-28, $\lambda_0 \approx 1313$ nm, if $\lambda_1 > 1313$ nm, $\Delta k_M < 0$; therefore, phase matching (Eq 3) in the NIR-III region can be achieved by adjusting Δk_{NL} through the pump power.

To provide a more comprehensive understanding of the FWM phenomenon, we will examine a more general case known as partially degenerate FWM [122], which occurs when two distinct incident optical frequency components ($\omega_i \neq \omega_j$) propagate through a Kerr medium. As these waves (ω_i and ω_j, where $\omega_j > \omega_i$) propagate into a fiber, the light intensity in the fiber will change as the frequency difference between these two waves $\Delta\omega = \omega_j - \omega_i$. Since the refractive index is linearly proportional to the optical intensity, it will

also follow this modulation at this frequency difference, which creates two additional frequency components (Figure 4b) at frequencies:

$$\omega_{ij} = \omega_i - (\omega_j - \omega_i) \tag{9}$$

$$\omega_{ji} = \omega_j + (\omega_j - \omega_i) . \tag{10}$$

The phase-matching condition for partially degenerate FWM [122]:

$$k = \tilde{\beta}_{ij} + \tilde{\beta}_{ji} - \tilde{\beta}_i - \tilde{\beta}_j + \gamma(P_i + P_j) = 0, \tag{11}$$

where P_i and P_j are incident pump optical powers at the fiber input.

In the case of a third wave with a different frequency ω_k propagating along with ω_i and ω_j in the fiber, this wave will be phase-modulated due to refractive index modulation. As a result, the additional wave is generated at frequency $\omega_{ijk} = \omega_i + \omega_j - \omega_k$. This case is named the non-degenerate FWM effect [122]. As one can see in Figure 4c, a large number of different generated frequencies are possible through permutations of initial frequencies (ω_i, ω_j, and ω_k). The new waves can occur at these frequencies only if the incident and generated waves satisfy phase-matching conditions:

$$\begin{aligned}
k_{ijk} &= \tilde{\beta}_{ijk} + \tilde{\beta}_k - \tilde{\beta}_i - \tilde{\beta}_j + \gamma(P_i + P_j + P_k) = 0, \\
k_{ikj} &= \tilde{\beta}_{ikj} + \tilde{\beta}_j - \tilde{\beta}_i - \tilde{\beta}_k + \gamma(P_i + P_k + P_j) = 0, \\
k_{iij} &= \tilde{\beta}_{iij} + \tilde{\beta}_j - \tilde{\beta}_i - \tilde{\beta}_i + \gamma(P_i + P_i + P_j) = 0, \\
&\quad \dots
\end{aligned} \tag{12}$$

Since FWM effect transfers energy from a strong pump to a signal at another frequency, it is commonly used as parametric amplification in fiber optic systems, such as fiber optical parametric amplifiers (FOPAs) and oscillators (FOPOs). In these systems, FWM leads to the interaction of pump pulses and signals. The control of the power and wavelength parameters facilitates the modulation and amplification of the signal at a new frequency.

For instance, R. Becheker et al. [56] designed a FOPO using a 7–15 m long dispersion shifted fiber (DSF) pumped by a mode-locked EDFL. Through the optimisation of pump power and dispersion in the FOPO incorporating a 3.45 m long SMF, they successfully generated 35 ps pulses with an average output power of ~15 mW, covering a wavelength range from 1617 nm to 1876 nm (Table 1, FWM).

2.2.3. SRS

In contrast to the Kerr effect, where there is no direct energy exchange between the electromagnetic field and the nonlinear dielectric medium, an
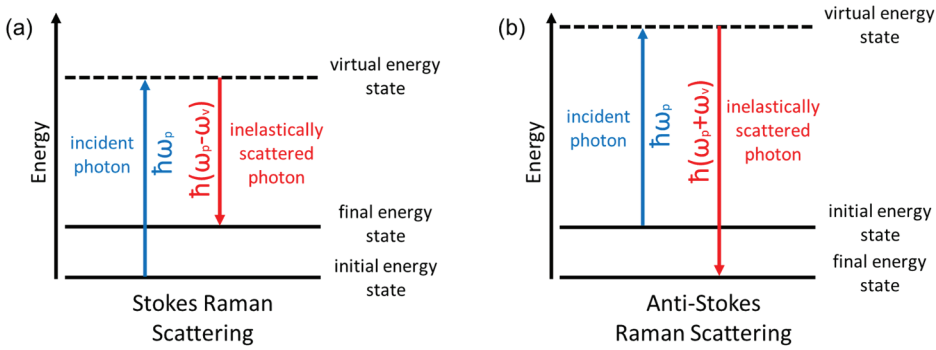
Figure 5. Schematic illustration of (a) Stokes and (b) Anti-Stokes Raman scattering.

inelastic-scattering phenomenon is characterised by transferring a portion of the field energy to the medium [31]. This phenomenon gives rise to SRS, linked to the excitation of vibrational modes in silica fibers.

The SRS effect involves the conversion of energy from a pump wave with a frequency ω_p to a lower-frequency Stokes wave ($\omega_s = \omega_p$-ω_v) (Figure 5a) and a higher-frequency anti-Stokes wave ($\omega_{as} = \omega_p$+ω_v) (Figure 5b), where ω_v represents a molecular vibrational frequency.

However, since the generation of an anti-Stokes wave requires that the medium is initially in an excited vibrational mode (Figure 5b), which has much less probability of occurring, anti-Stokes waves are much less powerful than Stokes ones [123]. The energy transfer to Stokes wave occurs within optical fibers only if the Raman gain power exceeds a threshold. In the case of standard fused silica fibers with a pump source operating at 1550 nm, the resulting probe signal (Stokes wave) undergoes a frequency shift to approximately 13.2 THz (113 nm).

The laser systems based on long silica fiber resonators can be combined with Raman gain to overcome fiber losses and achieve better laser efficiency in the NIR-III wavelength region. For example, X. Quan et al. [70] introduced a Raman gain into a 1699 nm CW TDFL system to stimulate SRS in a 4 km long SMF.

The original CW TDFL system with only TDF-based active gain combined a 2.7 m long TDF pumped by a 1565 nm laser source, a high-reflective fiber Bragg grating (HR FBG), and a 4 km long SMF for backward output (Figure 6a). The maximum output power reached a value of 0.33 W with a pump power of 21.5 W. The laser efficiency was limited to 1.5% due to high loss in the SMF and the limited emission cross-section of the TDF at this wavelength.

For the hybrid gain laser system with TDF-based active gain and Raman gain (Figure 6b), they used a 976 nm LD to pump EYDF, which was subsequently used as a 1565 nm Raman pump source. The first-order Stokes wave was redshifted from 1565 nm and overlapped with a broad emission spectrum
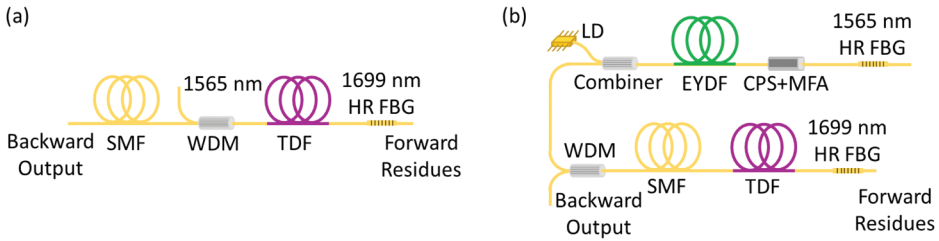
Figure 6. Schematic representation of thulium-doped fiber (TDF) lasers, operating at a wavelength of 1699 nm: (a) CW laser with an efficiency of 1.5% (only TDF-based active gain); (b) hybrid gain laser (with an additional Raman gain) operating at an unstable Q-switch or CW regime depending on pump power. The efficiency is 11.5% due to SRS in 4 km long single-mode fiber (SMF). (WDM – wavelength-division multiplexing; HR FBG – high reflectivity fiber Bragg grating; EYDF – Erbium/Ytterbium co-doped fiber; CPS+MFA – cladding power stripper and mode field adaptor). Adapted from [70] under terms of the CC-BY licence.

of the TDF, resulting in the energy transfer from this Raman pump to the amplification of the signal with a central wavelength of 1699 nm (Table 1, SRS, TDF). This combination of the Stokes waves and the emission spectrum of the TDF led to a significant boost in performance, resulting in an output power of about 2.5 W (efficiency of 11.5%) under the same 21.5 W pump power. When the pump power is around the lasing threshold (7.3 W), the hybrid gain laser runs in the unstable Q-switched regime with random pulse trains and varying repetition rates. However, with increased pump power (11.6 W), the temporal dynamics are strongly suppressed and turn into a CW regime. When the pump power is further increased (15.9–18.8 W), strongly modulated pulses dominate the CW background with few instantaneous high-intensity pulses.

Achieving an operating wavelength shift into the longer spectral range is possible by using gas-filled hollow-core photonic crystal fiber (HC-PCF) pumped by a 1550 nm EDFA [64]. This setup enabled the generation of nanosecond pulses within the wavelength range of 1693–1705 nm, facilitated by a frequency conversion stimulated in HC-PCF (Figure 7a).

If the first-order Stokes wave is sufficiently intensive, it can generate a second-order Stokes wave with the same frequency shift equal to the vibrational frequency. The further amplified second-order Stokes wave can then act as a source for generating higher-order Stokes waves far redshifted from the pump wavelength (Figure 3c). Figure 8 schematically represents the cascaded SRS.

H. Li et al. [63] demonstrated an example of cascaded SRS using a 10 m long H_2-filled HC-PCF pumped by a tunable EDFA operating in the 1540–1550 nm range. With a pump wavelength of 1540 nm, an average pump power of 5.3 W, a repetition rate of 2 MHz, and a gas pressure of 16 bar, the first-order Stokes light at 1693 nm achieved an output power of 3 W. However, the second-order Stokes light at 1801 nm was much weaker due to the limited pump power. It was also noted that using an excessively long fiber can
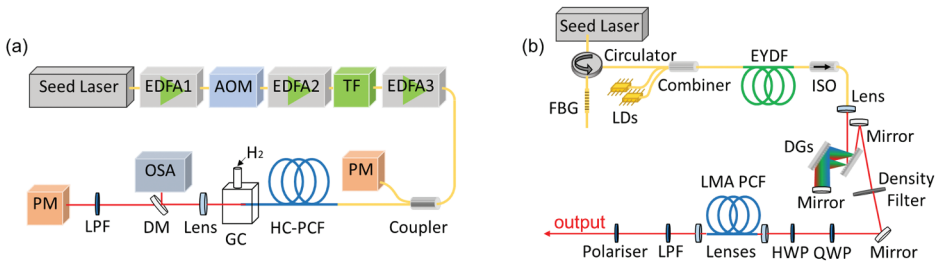
Figure 7. Schematic representation of (a) 15 ns-pulsed fiber laser based on SRS in H_2 gas-filled hollow-core photonic crystal fiber (HC-PCF), operating at 1693–1705 nm wavelength range with the output power of 3 W; (b) sub-100 fs-pulsed fiber laser based on SSFS in large mode area photonic crystal fiber (LMA PCF), operating at 1600–1700 nm with an output power of up to 114 mW. (EDFA – Erbium-doped fiber amplifier; EYDF – Erbium/Ytterbium co-doped fiber; AOM – acousto-optic modulator; TF – tunable fiber filter; PM – power meter; GC – gas cell; DM – dichroic mirror; OSA – optical spectrum analyser; LPF – long-pass filter; FBG – fiber Bragg grating; ISO – isolator; DG – dispersion grating; QWP – quarter-wave plate; HWP – half-wave plate). Adapted from [64] and [85] under terms of the CC-BY licence.
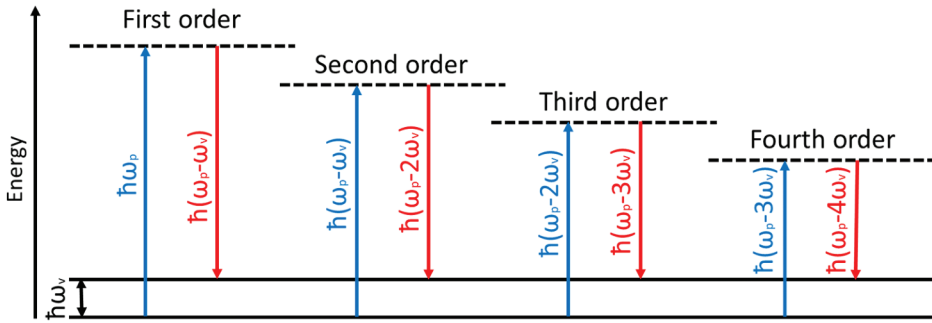
Figure 8. Schematic illustration of cascaded stimulated Raman scattering with first-, second-, third-, and fourth-order stokes waves.

redshift the laser operating wavelength further, increasing transmission losses and promoting second- and higher-order Raman conversion, which reduces the power of the first-order Raman signal.

2.2.4. SSFS

When pulses are characterised by short duration and broad spectrum, the Raman gain can selectively enhance the low-frequency components within the pulse by transferring energy from the higher-frequency parts of the same pulse. That process refers to intrapulse Raman scattering inside fiber [31].

The transfer of energy from high-frequency to low-frequency components of the pulses induces a progressive redshift in the pulse spectrum as it travels through the optical fiber. This nonlinear phenomenon is referred to as SSFS (Figure 3d) [118]. This effect can potentially move the operating wavelength of an EDFL into the wavelength range of 1600–1900 nm.

Nevertheless, noticeable spectral shifts resulting from SSFS occur when solitons propagate through SMFs with lengths extending to hundreds of meters.

In recent experiments, X. He et al. [90] demonstrated an all-fiber laser operating at 1696–1703 nm using a 460 m long polarisation-maintaining (PM) fiber. The laser consisted of two parts: an all-PM fiber NALM and a SSFS module. NALM included a $\pi/2$ phase shifter (a quarter-wave plate (QWP) surrounded by Faraday rotators and polarisers) and EDF pumped by 976 nm laser diodes. In the SSFS module, ultrashort pulses (a duration of 180 fs, an average power of 53 mW) after passing through long PM fiber converted from 1560 nm to 1700 nm pulses (a duration of 384 fs, an average power of 35 mW).

Another example of a widely tunable EDFL based on SSFS was demonstrated by A. Zach et al. [92]. They developed a 1480 nm cascaded Raman laser and a femtosecond pulsed PM EDF-based seed laser combined in an amplifier with a 3 m long Erbium-doped very large mode area (VLMA) PM fiber with a core diameter of 50 μm. The SSFS effect stimulated in VLMA fiber offered a wide wavelength tunability within the 1620–1990 nm range (Table 1, SSFS, EDF). This laser system generated sub-120 fs pulses with an average power of 1.6 W.

A similar laser system based on the SSFS effect in a large mode area photonic crystal fiber (LMA PCF) was demonstrated by D. Stoliarov et al. [85]. They developed an all-PM fiber mode-locked oscillator with a NALM and a preamplifier based on heavily EDF with an average power of 15 mW (Figure 7b). Then, the pulse was stretched from 2.3 ps to 40.6 ps in the fiber Bragg grating (FBG) stretcher and amplified in EYDF pumped by 980 nm laser diodes. After the amplification with a maximum output power of 1.2 W (pump power of 7 W), the pulse was compressed to 660 fs by a pair of free-space diffraction gratings. To redshift the central wavelength (1548 nm), the pulse was launched into a 1 m long LMA PCF. High-order solitons, propagating through LMA PCF, experienced perturbation inside the fiber, leading to the soliton fission phenomenon [118]. High-order solitons decayed into fundamental solitons of different widths. Intrapulse Raman scattering led to the SSFS effect, shifting the highest-order fundamental soliton central wavelength. At a pump power of 221 mW, the central wavelength of the output spectrum was at 1625 nm with a soliton duration of 165 fs and an average power of 55 mW. However, with anomalous dispersion, the SSFS effect is more significant for the shortest solitons, expanding the pulse spectrum to the red side. The increase in pump power (up to 321 mW) influenced the SSFS, causing a gradual reduction of the pulse duration and shifting towards a longer wavelength of 1700 nm, accompanied by an average output power of 107 mW, while the pulse duration reduced to 91 fs.

Fiber lasers based on the SSFS effect exhibit notable characteristics such as high-power spectral density and a wide wavelength tuning range. Nonetheless, their advancement presents challenges in effectively managing system dispersion and required output parameters.

2.2.5. SC

When the high-power ultrashort pulses are launched into a fiber characterised by a small anomalous dispersion ($\beta_2 <0$), it leads to a significant spectral broadening, which is a consequence of the interplay between the SPM, FWM, and SRS effects [31]. Their combination creates a cascading effect where new spectral components are continuously generated, leading to a substantial increase in bandwidth.

When pulses with large enough power are launched into the HNLF, they initiate high-order solitons. These solitons propagating through the fiber can experience fission due to the perturbed effect of third- and higher-order dispersion, forming fundamental solitons with different spectral widths and temporal durations. In the presence of intrapulse Raman scattering, these solitons experience a deceleration and expand the spectrum, propagating through the fiber with distinctive velocities that depend on their duration. This effect amplifies the low-frequency components of a pulse, transferring energy from high-frequency components. That results in the continuous shift of the pulse spectrum towards a red side as the pulse propagates the fiber.

At the same time, if soliton fission occurs in the anomalous dispersion close to the zero-dispersion wavelength of the medium, a transfer of a portion of the pulse energy to dispersive waves at frequencies that satisfy a phase-matching condition can be observed. The dispersive waves, generated in the time domain behind the solitons, can collide with decelerating solitons. Due to the FWM effect, this interaction generates new dispersive waves at different frequencies in normal dispersion, further broadening the initial pulse spectrum to the blue side. This extreme broadening can lead to the generation of SC extending up to 50 THz on both sides of the spectrum (Figure 3e) [118].

SC fiber laser configurations are able to provide nonlinear optical broadening with high spectral density and flatness [124]. That is one of the most common techniques to obtain a pulse generation in the NIR-III.

For instance, J. Takayanagi et al. [102] developed an octave-spanning SC in a 980–2570 nm spectral region (Table 1, SC, EDF). The key element of the laser system was a PM highly nonlinear dispersion-shifted fiber (HN-DSF). This fiber compressed the pulses by adjusting the group velocity dispersion between the EDF and SMF. The output achieved sub-50 fs pulses with a peak power of 42.3 kW.

Another example of a SC element is highly nonlinear fibers (HNLFs) [7,96–99,103,125]. X. Li et al. [97] demonstrated a SC source with a wideband of 370 nm. They used an EDF-based seed laser coupled into an intensity

modulator and amplified by two-stage EDFAs. As a result, a SC laser with a single-/dual-pulse repetition rate between 170 MHz and 2 GHz and a pulse duration of 60–180 ps was obtained.

This nonlinear effect can also be realised by incorporating a PCF into the laser system [101,109,126,127], as presented in a BEDFL source by N.S. Shahabuddin et al. [109]. The laser system with a 100 m long PCF generated femtosecond pulses with a repetition rate of about 40 MHz in the SC spectrum ranging from 1250 nm to 1910 nm (Table 1, SC, BEDF).

Wide spectral coverage, compactness, high power, and coherent properties allow SC lasers to be used as versatile light sources for applications such as microscopy and spectroscopy. The ultra-broadband spectrum offers the opportunity to increase the resolution of imaging up to several microns [128].

However, their complexity and higher cost due to alignment requirements create problems in their implementation in biomedicine. A significant limitation of SC laser sources is the amplification of even minor instabilities originating from the seed laser. This behaviour increases white noise and restricts the application of SC sources for measuring and imaging biological tissues with a weak signal [129].

3. Discussion and conclusions

Ultrashort pulsed NIR-III fiber lasers are crucial for different applications, and the choice of design methods depends on the specific parameters required for the intended use. For applications where a wide tuning range is not required, fiber lasers based on only BDF or rare-earth-doped fibers are optimal for system design. These doped fibers and various fiber structures have demonstrated the ability to cover almost the entire NIR-III spectral range (Table 1, PI).

Recent advances include Erbium-doped phosphate [130], Bismuth-doped aluminosilicate/germanosilicate [115,131], and fluoride/W-type/depressed-cladding Thulium-doped fibers that exhibit broad emission bands in the 1420–1680 nm, 1600–1700 nm, and 1600–1900 nm ranges, respectively. These novel doped fibers present significant potential for mode-locking generation in fiber lasers.

However, despite these advances, the availability of commercial gain medium fibers emitting in the NIR-III spectral range remains limited, posing challenges in developing fiber lasers and amplifiers without implementing nonlinear effect methods for wavelength shifting in fibers.

Different nonlinear-based techniques (SPM, FWM, SRS, SSFS, and SC) reviewed in that paper have advantages and disadvantages:

- SPM

  In SPM-based methods, a high peak power signal passing through a HNLF experiences not only spectral broadening but also changes in pulse duration. Therefore, users of the SPM technique must compress the pulses. This can be achieved by implementing either hundreds of meters of SMF or diffraction gratings [45]. However, to obtain short pulses (<500 fs), it is necessary to stretch the pulses before their amplification in the active fiber to reduce nonlinear effects. Consequently, a balance must be found between pulse duration and spectral broadening.

  Additionally, to achieve higher pulse energy (>100 pJ), significant modifications to the active fiber are required, such as the development of LMA fibers. These modifications are essential for optimising the performance of the fiber laser system while maintaining the desired pulse characteristics.

- FWM

  The method of wavelength shifting based on FWM, is commonly used in FOPA and FOPO systems. This technique is highly effective in achieving broad wavelength tunability (>250 nm [56]). However, the relatively low nonlinear properties of the used fibers limit the realisation of higher optical parametric amplification gain and overall laser efficiency. Therefore, the development and implementation of new HNLFs can significantly improve this method.

- SRS

  SRS is one of the most popular techniques for redshifting a laser operating wavelength. Despite significant advancements in wavelength tunability (1550–1740 nm [132]), most developments have focused on continuous-wave fiber lasers. Ultrafast pulsed lasers often exhibit low efficiency in the NIR-III spectral region, and SRS-based lasers typically have complex structural designs involving gas-filled fibers and free-space elements [62–66]. Further research is needed to enhance the stability and efficiency of these fiber lasers.

- SSFS

  Laser systems based on the SSFS effect demonstrate high tunability and duration. However, the relatively high nonlinearity of the SMF limits the pulse energy to less than 1 nJ. The use of fibers with low nonlinearity parameters can significantly improve laser systems in the NIR-III range. For example, hollow-core or large mode area PCFs allow the generation of pulses with high energy (10 nJ [85], 44.8 nJ [81,82]), while the last

ones have the advantages of low bending loss and significant wavelength shift tuning.

- SC
  SC lasers, based on the combination of several nonlinear effects in optical fibers, are characterised by extremely high tunability, reaching wavelength ranges of 630 nm [110] and 885 nm [107]. However, SC sources often have a complex design and low pulse energy. Since small instabilities in the seed laser can be amplified, creating white noise, the development of stable master oscillators is necessary for the advancement of SC laser technology.

A significant amount of recent research on ultrashort pulse NIR-III fiber lasers demonstrates their high demand in various applications. Despite significant progress, the laser systems still require improvements. Continued study and advancements in this area will undoubtedly lead to the development of laser systems featuring broader tunability, higher efficiency, and increased pulse energy to meet the growing needs of scientific and industrial applications.

Disclosure statement

No potential conflict of interest was reported by the author(s).

ORCID

Diana Galiakhmetova http://orcid.org/0000-0002-6222-2122

References

[1] Hemmer E, Benayas A, Légaré F, et al. Exploiting the biological windows: current perspectives on fluorescent bioprobes emitting above 1000 nm. Nanoscale Horiz. 2016;1:168–184. doi: 10.1039/C5NH00073D

[2] Golovynskyi S, Golovynska I, Stepanova LI, et al. Optical windows for head tissues in near-infrared and short-wave infrared regions: approaching transcranial light applications. J Biophotonics. 2018;11:e201800141. doi: 10.1002/jbio.201800141

[3] Galiakhmetova D, Dremin V, Koviarov A, et al. Ultra-short laser pulses propagation through mouse head tissues: experimental and computational study. IEEE J Select Top Quantum Electron. 2023;29:1–11. doi: 10.1109/JSTQE.2022.3214788

[4] Xia F, Wu C, Sinefeld D, et al. In vivo label-free confocal imaging of the deep mouse brain with long-wavelength illumination. Biomed Opt Express. 2018;9:6545–6555. doi: 10.1364/BOE.9.006545

[5] Cheng H, Tong S, Deng X, et al. Deep-brain 2-photon fluorescence microscopy in vivo excited at the 1700 nm window. Opt Lett. 2019;44:4432–4435. doi: 10.1364/OL.44.004432

[6] Roy S, Gord JR, Patnaik AK. Recent advances in coherent anti-stokes raman scattering spectroscopy: fundamental developments and applications in reacting flows. Prog Energy Combust Sci. 2010;36:280–306. doi: 10.1016/j.pecs.2009.11.001

[7] Freudiger CW, Yang W, Holtom GR, et al. Stimulated raman scattering microscopy with a robust fibre laser source. Nat Photon. 2014;8:153–159. doi: 10.1038/nphoton.2013.360

[8] Yamanaka M, Hayakawa N, Nishizawa N. High-spatial-resolution deep tissue imaging with spectral-domain optical coherence microscopy in the 1700-nm spectral band. J Biomed Opt. 2019;24:1–4. doi: 10.1117/1.JBO.24.7.070502

[9] Kurilchik S, Gacci M, Cicchi R, et al. Advanced multimodal laser imaging tool for urothelial carcinoma diagnosis (AMPLITUDE). J Phys Photonics. 2020;2:021001. doi: 10.1088/2515-7647/ab7bab

[10] Crotti C, Deloison F, Alahyane F, et al. Wavelength optimization in femtosecond laser corneal surgery. Invest Ophthalmol Vis Sci. 2013;54:3340–3349. doi: 10.1167/iovs.12-10694

[11] Phelan R, Byrne D, O'Carroll J, et al. Mid-Infrared InP-Based Discrete Mode Laser Diodes. Optical Fiber Appl. 2019;15. doi: 10.5772/intechopen.86458

[12] Jeong S-H, Mizumoto T, Takenaka M, et al. All-optical wavelength conversion in a GaInAsPInP optical gate loaded with a Bragg reflector. Appl Opt. 2003;42:6672–6677. doi: 10.1364/AO.42.006672

[13] Guina M, Rantamäki A, Härkönen A. Optically pumped VECSELs: review of technology and progress. J Phys D: Appl Phys. 2017;50:383001. doi: 10.1088/1361-6463/aa7bfd

[14] Krauth J, Steinmann A, Hegenbarth R, et al. Broadly tunable femtosecond near- and mid-ir source by direct pumping of an OPA with a 417 MHz Yb: KGW oscillator. Opt Express. 2013;21:11516–11522. doi: 10.1364/OE.21.011516

[15] Marshall LR, Kasinski J, Hays AD, et al. Efficient optical parametric oscillator at 16 μm. Opt Lett. 1991;16:681–683. doi: 10.1364/OL.16.000681

[16] Linnenbank H, Linden S. High repetition rate femtosecond double pass optical parametric generator with more than 2 W tunable output in the NIR. Opt Express. 2014;22:18072–18077. doi: 10.1364/OE.22.018072

[17] Meng X, Wang Z, Tian W, et al. Watt-level widely tunable femtosecond mid-infrared KTiOAsO 4 optical parametric oscillator pumped by a 103 μm Yb: KGW laser. Opt Lett. 2018;43:943–946. doi: 10.1364/OL.43.000943

[18] Mörz F, Steinle T, Steinmann A, et al. Multi-watt femtosecond optical parametric master oscillator power amplifier at 43 MHz. Opt Express. 2015;23:23960–23967. doi: 10.1364/OE.23.023960

[19] Braunstein R. Nonlinear optical effects. Phys Rev. 1962;125:475. doi: 10.1103/PhysRev.125.475

[20] Günter P. Nonlinear optical effects and materials. Berlin, Heidelberg: Springer; 2012;72. doi: 10.1007/978-3-540-49713-4

[21] Joseph RM, Taflove A. FDTD Maxwell's equations models for nonlinear electrodynamics and optics. IEEE Trans Antennas Propag. 1997;45:364–374. doi: 10.1109/8.558652

[22] Byer RL, Piskarskas A. Optical parametric oscillation and amplification introduction. JOSA B. 1993;10:2148–2150. doi: 10.1364/JOSAB.10.002148

[23] Powers PE. Field guide to nonlinear optics. 2013. doi: 10.1117/3.1002081

[24] E HS. Tunable optical parametric oscillators. Proc IEEE. 1969;57:2096–2113. doi: 10.1109/PROC.1969.7495

[25] Tzeng Y-W, Huang C-H, Lin Y-Y, etal. High repetition rate optical parametric amplification based on a single Yb: fiber laser. Conf On Lasers Electro-Optics/int Quantum Electron Conf (Optical Soc Of Am). 2009:CWJ7. doi: 10.1364/CLEO.2009.CWJ7

[26] Kiani L, Lu T, Sharping JE. Comparison of amplitude noise of a fiber-optical parametric oscillator and a supercontinuum source. J Opt Soc Am B. 2014;31:1986–1990. doi: 10.1364/JOSAB.31.001986

[27] O'Connor MV, Watson MA, Shepherd DP, et al. Synchronously pumped optical parametric oscillator driven by a femtosecond mode-locked fiber laser. Opt Lett. 2002;27:1052–1054. doi: 10.1364/OL.27.001052

[28] Kirchner M, Niedringhaus A, Durfee C, et al. Ultrafast optical parametric oscillator pumped by an all normal dispersion (ANDi) Yb: fiber oscillator. 2012 Conference on Lasers and Electro-Optics (CLEO). 2012:1–2. doi: 10.1364/CLEO_SI.2012.CM1B.1

[29] Xu L, Feehan JS, Shen L, et al. Yb-fiber amplifier pumped idler-resonant PPLN optical parametric oscillator producing 90 femtosecond pulses with high beam quality. Appl Phys B. 2014;117:987–993. doi: 10.1007/s00340-014-5918-7

[30] Fan J, Gu C, Zhao J, et al. Dielectric-mirror-less femtosecond optical parametric oscillator with ultrabroad-band tunability. Opt Lett. 2018;43:2316–2319. doi: 10.1364/OL.43.002316

[31] Agrawal GP Nonlinear fiber optics Nonlinear Science at the Dawn of the 21st Century. Lecture Notes in Physics. Berlin, Heidelberg: Springer. 2000;542:195–211. doi: 10.1007/3-540-46629-0_9

[32] Noronen T, Firstov S, Dianov E, et al. 1700 nm dispersion managed mode-locked bismuth fiber laser. Sci Rep. 2016;6:24876. doi: 10.1038/srep24876

[33] Yusoff NM, Chyi JLY, Ng EK, et al. Bulk α-alumina embedded tapered fiber as Q-switcher in an erbium-doped fiber laser. Phys Scr. 2024;99:065522. doi: 10.1088/1402-4896/ad447f

[34] Zhang H, Bao Q, Tang D, et al. Large energy soliton erbium-doped fiber laser with a graphene-polymer composite mode locker. Appl Phys Lett. 2009;95. doi: 10.1063/1.3244206

[35] Dai M, Liu B, Ma Y, et al. GHz fundamental mode-locking of a highly integrated Er-doped all-fiber ring laser. arXiv preprint arXiv:2411.16059. 2024. doi: 10.48550/arXiv.2411.16059

[36] Noronen T, Okhotnikov O, Gumenyuk R. Electronically tunable thulium-holmium mode-locked fiber laser for the 1700–1800 nm wavelength band. Opt Express. 2016;24:14703–14708. doi: 10.1364/OE.24.014703

[37] Li C, Wei X, Kong C, et al. Fiber chirped pulse amplification of a short wavelength mode-locked thulium-doped fiber laser. APL Photonics. 2017;2. doi: 10.1063/1.4996441

[38] Emami SD, Dashtabi MM, Lee HJ. 1700 nm and 1800 nm band tunable thulium doped mode-locked fiber lasers. Sci Rep. 2017;7:12747. doi: 10.1038/s41598-017-13200-x

[39] Emami SD, Khodaei A, Gandan S, et al. Thulium-doped fiber laser utilizing a photonic crystal fiber-based optical low-pass filter with application in 17 μm and 18 μm band. Opt Express. 2015;23:19681–19688. doi: 10.1364/OE.23.019681

[40] Chen J-X, Li X-Y, Li T-J, et al. 1.7-μm dissipative soliton Tm-doped fiber laser. Photonics Res. 2021;9:873–878. doi: 10.1364/PRJ.419273

[41] Liu X, Sahu JK, Gumenyuk R. Tunable dissipative soliton Tm-doped fiber laser operating from 1700 nm to 1900 nm. Opt Lett. 2023;48:612–615. doi: 10.1364/OL.478838

[42] Li C, Shi J, Wang X, et al. High-energy all-fiber gain-switched thulium-doped fiber laser for volumetric photoacoustic imaging of lipids. Photonics Res. 2020;8:160–164. doi: 10.1364/PRJ.379882

[43] Liu X, Gumenyuk R. Wavelength-tunable chirped pulse amplification system (1720 nm–1800 nm) based on thulium-doped fiber. Photonics. 2024;11:11. doi: 10.3390/photonics11050439

[44] Khegai AM, Melkumov MA, Riumkin KE, et al. Mode-locked bismuth fiber laser operating at 1.7 μm based on NALM. Laser Applications Conference (Optica Publishing Group). 2017;JTu2A–20. doi: 10.1364/ASSL.2017.JTu2A.20

[45] Khegai A, Melkumov M, Riumkin K, et al. Nalm-based bismuth-doped fiber laser at 1.7 μm. Opt Lett. 2018;43:1127–1130. doi: 10.1364/OL.43.001127

[46] Zhang H, Xia H, Fan M, et al. Observation of wavelength tuning in a mode-locked figure-9 fiber laser. Photonics. 2023;10:184. doi: 10.3390/photonics10020184

[47] Yamanaka M, Kawagoe H, Nishizawa N. High-power supercontinuum generation using high-repetition-rate ultrashort-pulse fiber laser for ultrahigh-resolution optical coherence tomography in 1600 nm spectral band. Appl Phys Express. 2016;9:022701. doi: 10.7567/APEX.9.022701

[48] Yamanaka M, Teranishi T, Kawagoe H, et al. Optical coherence microscopy in 1700 nm spectral band for high-resolution label-free deep-tissue imaging. Sci Rep. 2016;6:31715. doi: 10.1038/srep31715

[49] Ishida S, Nishizawa N. Quantitative comparison of contrast and imaging depth of ultrahigh-resolution optical coherence tomography images in 800–1700 nm wavelength region. Biomed Opt Express. 2012;3:282–294. doi: 10.1364/BOE.3.000282

[50] Chung H-Y, Liu W, Cao Q, et al. Er-fiber laser enabled, energy scalable femtosecond source tunable from 13 to 17 μm. Opt Express. 2017;25:15760–15771. doi: 10.1364/OE.25.015760

[51] Chen S, Chen Y, Liu K, et al. All-fiber short-wavelength tunable mode-locked fiber laser using normal dispersion thulium-doped fiber. Opt Express. 2020;28:17570–17580. doi: 10.1364/OE.395167

[52] Chen S, Chen Y, Liu K, et al. W-type normal dispersion thulium-doped fiber-based high-energy all-fiber femtosecond laser at 1.7 μm. Opt Lett. 2021;46:3637–3640. doi: 10.1364/OL.431023

[53] Zhou Y, Cheung KKY, Yang S, et al. Ultra-widely tunable, narrow linewidth picosecond fiber-optical parametric oscillator. IEEE Photonics Technol Lett. 2010;22:1756–1758. doi: 10.1109/LPT.2010.2085078

[54] Zhou Y, Cheung KKY, Yang S, et al. Widely tunable picosecond optical parametric oscillator using highly nonlinear fiber. Opt Lett. 2009;34:989–991. doi: 10.1364/OL.34.000989

[55] Tang M, Becheker R, Hanzard P-H, et al. Low noise high-energy dissipative soliton erbium fiber laser for fiber optical parametric oscillator pumping. Appl Sci. 2018;8:2161. doi: 10.3390/app8112161

[56] Becheker R, Tang M, Hanzard P-H, et al. High-energy dissipative soliton-driven fiber optical parametric oscillator emitting at 1.7 μm. Laser Phys Lett. 2018;15:115103. doi: 10.1088/1612-202X/aadfcd

[57] Li K, Huang Q, Jiang J, et al. Wavelength-tunable L-band high repetition rate erbium-doped fiber laser based on dissipative four-wave mixing. Sensors. 2021;21:5975. doi: 10.3390/s21175975

[58] Qin Y, Batjargal O, Cromey B, et al. All-fiber high-power 1700 nm femtosecond laser based on optical parametric chirped-pulse amplification. Opt Express. 2020;28:2317–2325. doi: 10.1364/OE.384185

[59] Qin Y, Batjargal O, Cromey B, et al. High-power 1700 nm femtosecond laser based on optical parametric chirped-pulse amplification. 2020 Conference on Lasers and Electro-Optics (CLEO) 10-15 May 2020 San Jose, CA, USA. IEEE. 2020;1–2. doi: 10.1364/CLEO_SI.2020.STh1P.5

[60] Li C, Chen N, Wei X, et al. High-power widely tunable all-fiber thulium-assisted optical parametric oscillator at SWIR band. Opt Lett. 2016;41:5258–5261. doi: 10.1364/OL.41.005258

[61] Zhdanov I, Volosi VM, Koliada NA, et al. Raman dissipative soliton source of ultrashort pulses in NIR-III spectral window. Opt Express. 2023;31:35156–35163. doi: 10.1364/OE.499249

[62] Huang W, Li Z, Cui Y, et al. Efficient, watt-level, tunable 1.7 μm fiber Raman laser in H 2-filled hollow-core fibers. Opt Lett. 2020;45:475–478. doi: 10.1364/OL.378496

[63] Li H, Huang W, Cui Y, et al. Pure rotational stimulated raman scattering in H 2-filled hollow-core photonic crystal fibers. Opt Express. 2020;28:23881–23897. doi: 10.1364/OE.396621

[64] Li H, Pei W, Huang W, et al. Highly efficient nanosecond 1.7 μm fiber gas raman laser by H2-filled hollow-core photonic crystal fibers. Cryst (Basel). 2020;11:32. doi: 10.3390/cryst11010032

[65] Pei W, Li H, Huang W, et al. All-fiber tunable pulsed 1.7 μm fiber lasers based on stimulated raman scattering of hydrogen molecules in hollow-core fibers. Molecules. 2021;26:4561. doi: 10.3390/molecules26154561

[66] Pei W, Li H, Huang W, et al. Pulsed fiber laser oscillator at 1.7 μm by stimulated raman scattering in H 2-filled hollow-core photonic crystal fibers. Opt Express. 2021;29:33915–33925. doi: 10.1364/OE.440461

[67] Grimes A, Hariharan A, Sun Y, et al. Hundred-watt CW and Joule level pulsed output from raman fiber laser in 1.7-μm band fiber lasers XVII. Technol And Syst. 2020;11260:234–239. doi:10.1117/12.2545034

[68] Zhdanov IS, Bednyakova AE, Volosi VM, et al. Energy scaling of an erbium-doped mode-locked fiber laser oscillator. OSA Continuum. 2021;4:2663–2670. doi: 10.1364/OSAC.441262

[69] Vazquez-Zuniga L, Jeong Y. Super-broadband noise-like pulse erbium-doped fiber ring laser with a highly nonlinear fiber for raman gain enhancement. IEEE Photonics Technol Lett. 2012;24:1549–1551. doi: 10.1109/LPT.2012.2208451

[70] Quan X, Ma R, Wu H, et al. Low threshold and high spectral purity 1.7 μm random fiber laser based on hybrid gain. Opt Laser Technol. 2022;155:108410. doi: 10.1016/j.optlastec.2022.108410

[71] Yang H, Zhang R, Jiang X, et al. 1.7 μm-1.73 μm tunable ultrafast Raman fiber laser pumped by 1.6 μm dissipative soliton pulses. Opt Express. 2022;30:45970–45979. doi: 10.1364/OE.476204

[72] Castellani CES, Kelleher EJR, Travers JC, et al. Ultrafast raman laser mode-locked by nanotubes. Opt Lett. 2011;36:3996–3998. doi: 10.1364/OL.36.003996

[73] Korolev AE, Kuksenkov DV, Nazarov VN. Controllable self-frequency shift of subpicosecond soliton light pulses in a nonlinear optical fiber. Opt Spectrosc. 2007;102:86–89. doi: 10.1134/S0030400X0701016X

[74] Nishizawa N, Goto T. Compact system of wavelength-tunable femtosecond soliton pulse generation using optical fibers. IEEE Photon Technol Lett. 1999;11:325–327. doi: 10.1109/68.748223

[75] Soboń G, Martynkien T, Tarnowski K, et al. Generation of sub-100 fs pulses tunable from 1700 to 2100 nm from a compact frequency-shifted Er-fiber laser. Photon Res. 2017;5:151–155. doi: 10.1364/PRJ.5.000151

[76] Tauser F, Adler F, Leitenstorfer A. Widely tunable sub-30-fs pulses from a compact erbium-doped fiber source. Opt Lett. 2004;29:516–518. doi: 10.1364/OL.29.000516

[77] Nishizawa N, Goto T. Widely wavelength-tunable ultrashort pulse generation using polarization maintaining optical fibers. IEEE J Sel Top Quantum Electron. 2001;7:518–524. doi: 10.1109/2944.974222

[78] Chestnut DA, Taylor JR. Soliton self-frequency shift in highly nonlinear fiber with extension by external raman pumping. Opt Lett. 2003;28:2512–2514. doi: 10.1364/OL.28.002512

[79] Liu X, Xu C, Knox WH, et al. Soliton self-frequency shift in a short tapered air–silica microstructure fiber. Opt Lett. 2001;26:358–360. doi: 10.1364/OL.26.000358

[80] Takayanagi J, Sugiura T, Yoshida M. 1.0–1.7-μm wavelength-tunable ultrashort-pulse generation using femtosecond Yb-doped fiber laser and photonic crystal fiber. IEEE Photonics Technol Lett. 2006;18:2284–2286. doi: 10.1109/LPT.2006.884891

[81] Wang K, Xu C. Tunable high-energy soliton pulse generation from a large-mode-area fiber and its application to third harmonic generation microscopy. Appl Phys Lett. 2011;99. doi: 10.1063/1.3628337

[82] Wang K, Horton NG, Charan K, et al. Advanced fiber soliton sources for nonlinear deep tissue imaging in biophotonics. IEEE J Select Top Quantum Electron. 2014;20:50–60. doi: 10.1109/JSTQE.2013.2276860

[83] Wang K, Xu C. Wavelength-tunable high-energy soliton pulse generation from a large-mode-area fiber pumped by a time-lens source. Opt Lett. 2011;36:942–944. doi: 10.1364/OL.36.000942

[84] Nguyen TN, Kieu K, Churin D, et al. High power soliton self-frequency shift with improved flatness ranging from 1.6 to 1.78 μm. IEEE Photonics Technol Lett. 2013;25:1893–1896. doi: 10.1109/LPT.2013.2279239

[85] Stoliarov D, Koviarov A, Korobko D, et al. Fibre laser system with wavelength tuning in extended telecom range. Optical Fiber Technol. 2022;72:102994. doi: 10.1016/j.yofte.2022.102994

[86] Fang X, Wang Z, Zhan L. Efficient generation of all-fiber femtosecond pulses at 1.7 μm via soliton self-frequency shift. Optical Eng. 2017;56:046107. doi: 10.1117/1.OE.56.4.046107

[87] Delahaye H, Hage CH, Bardet SM, et al. Generation of megawatt soliton at 1680 nm in very large mode area antiresonant fiber and application to three-photon microscopy. J Opt. 2021;23:115504. doi: 10.1088/2040-8986/ac26cf

[88] Horton NG, Wang K, Kobat D, et al. In vivo three-photon microscopy of subcortical structures within an intact mouse brain. Nat Photon. 2013;7:205–209. doi: 10.1038/nphoton.2012.336

[89] Ruan Q, Luo Z, Wan X, et al. 1.61–1.85 μm tunable all-fiber raman soliton source using a phosphor-doped fiber pumped by 1.56 μm dissipative solitons. IEEE Photonics J. 2017;9:1–7. doi: 10.1109/JPHOT.2017.2657760

[90] He X, Lin Q, Guo H, et al. Robust 1.7-μm, all-polarization-maintaining femtosecond fiber laser source based on standard telecom fibers. Appl Phys Express. 2019;12:072007. doi: 10.7567/1882-0786/ab266f

[91] Cadroas P, Abdeladim L, Kotov L, et al. All-fiber femtosecond laser providing 9 nJ, 50 MHz pulses at 1650 nm for three-photon microscopy. J Optics. 2017;19:065506. doi: 10.1088/2040-8986/aa6f72

[92] Zach A, Mohseni M, Polzer C, et al. All-fiber widely tunable ultrafast laser source for multimodal imaging in nonlinear microscopy. Opt Lett. 2019;44:5218–5221. doi: 10.1364/OL.44.005218

[93] Nicholson JW, Desantolo A, Kaenders W, et al. Self-frequency-shifted solitons in a polarization-maintaining, very-large-mode area, Er-doped fiber amplifier. Opt Express. 2016;24:23396–23402. doi: 10.1364/OE.24.023396

[94] Sun M, Cui J, Yu B, et al. High-power, sub-100-fs, 1600–1700-nm all-fiber laser for deep multiphoton microscopy. Opt Express. 2023;31:24298–24306. doi: 10.1364/OE.493694

[95] Swiderski J, Maciejewska M. The generation of a broadband, spectrally flat supercontinuum extended to the mid-infrared with the use of conventional passive single-mode fibers and thulium-doped single-mode fibers pumped by 1.55 μm pulses. Laser Phys Lett. 2012;10:015106. doi: 10.1088/1612-2011/10/1/015106

[96] Zhang P, Wu D, Li X, et al. 1.7 μm tunable picosecond-pulsed fiber light source based on nonlinear effect combination using a cascaded intensity modulator. Laser Phys. 2018;28:095101. doi: 10.1088/1555-6611/aac7e7

[97] Li X, Zhang P, Wu D, et al. Single-/dual-pulse repetition rate variable supercontinuum light source with peak wavelength around 1.7 μm using a modulated pump. Appl Opt. 2020;59:3458–3466. doi: 10.1364/AO.387225

[98] Luo X, Tuan TH, Suzuki T, et al. Intracavity supercontinuum generation in a mode-locked erbium-doped fiber laser based on the mamyshev mechanism with highly nonlinear fiber. Opt Lett. 2020;45:2530–2533. doi: 10.1364/OL.389779

[99] Kawagoe H, Ishida S, Aramaki M, et al. Development of a high power supercontinuum source in the 17 μm wavelength region for highly penetrative ultrahigh-resolution optical coherence tomography. Biomed Opt Express. 2014;5:932–943. doi: 10.1364/BOE.5.000932

[100] Ishida S, Nishizawa N, Ohta T, et al. Ultrahigh-resolution optical coherence tomography in 1.7 μm region with fiber laser supercontinuum in low-water-absorption samples. Appl Phys Express. 2011;4:052501. doi: 10.1143/APEX.4.052501

[101] Liao R, Song Y, Zhou X, et al. Ultra-flat supercontinuum generated from high-power, picosecond telecommunication fiber laser source. Appl Opt. 2016;55:9384–9388. doi: 10.1364/AO.55.009384

[102] Takayanagi J, Nishizawa N, Nagai H, et al. Generation of high-power femtosecond pulse and octave-spanning ultrabroad supercontinuum using all-fiber system. IEEE Photonics Technol Lett. 2005;17:37–39. doi: 10.1109/LPT.2004.837741

[103] Kieu K, Jones RJ, Peyghambarian N. High power femtosecond source near 1 micron based on an all-fiber Er-doped mode-locked laser. Opt Express. 2010;18:21350–21355. doi: 10.1364/OE.18.021350

[104] Song R, Hou J, Chen SP, et al. Near-infrared supercontinuum generation in an all-normal dispersion MOPA configuration above one hundred watts. Laser Phys Lett. 2012;10:015401. doi: 10.1088/1612-2011/10/1/015401

[105] Song R, Hou J, Chen S, et al. High power supercontinuum generation in a nonlinear ytterbium-doped fiber amplifier. Opt Lett. 2012;37:1529–1531. doi: 10.1364/OL.37.001529

[106] Jiang L, Song R, He J, et al. 714 W all-fiber supercontinuum generation from an ytterbium-doped fiber amplifier. Opt Laser Technol. 2023;161:109168. doi: 10.1016/j.optlastec.2023.109168

[107] Alcántara-Bautista U, Durán-Sánchez M, Addiel Espinosa-De-La-Cruz E, et al. Intracavity ultra-broad supercontinuum generation from a figure-9 Yb-doped fiber laser. Opt Laser Technol. 2024;168:110016. doi: 10.1016/j.optlastec.2023.110016

[108] Cruz EAEL, Durán-Sánchez M, Pottiez O, et al. Ultra-flat supercontinuum generation in an all-fiber self-Q-switched Er/Yb laser. IEEE Photon Technol Lett. 2023;35:454–457. doi: 10.1109/LPT.2023.3254369

[109] Shahabuddin NS, Awang NA, Ahmad H, et al. Supercontinuum generation using a passive mode-locked stretched-pulse bismuth-based erbium-doped fiber laser. Opt Laser Technol. 2012;44:741–743. doi: 10.1016/j.optlastec.2011.11.039

[110] Zeng J, Akosman AE, Sander MY. Supercontinuum generation from a thulium ultrafast fiber laser in a high NA silica fiber. IEEE Photon Technol Lett. 2019;31:1787–1790. doi: 10.1109/LPT.2019.2946835

[111] Thipparapu NK, Wang Y, Wang S, et al. Bi-doped fiber amplifiers and lasers [invited]. Opt Mater Express. 2019;9:2446–2465. doi: 10.1364/OME.9.002446

[112] Firstov SV, Alyshev SV, Riumkin KE, et al. Laser-active fibers doped with bismuth for a wavelength region of 1.6–1.8 μm. IEEE J Select Top Quantum Electron. 2018;24:1–15. doi: 10.1109/JSTQE.2018.2801461

[113] Bufetov IA, Dianov EM. Bi-doped fiber lasers. Laser Phys Lett. 2009;6:487. doi: 10.1002/lapl.200910025

[114] Bufetov IA, Melkumov MA, Firstov SV, et al. Bi-doped optical fibers and fiber lasers. IEEE J Sel Top Quantum Electron. 2014;20:111–125. doi: 10.1109/JSTQE.2014.2312926

[115] Wang Y, Wang S, Halder A, et al. (INVITED) Bi-doped optical fibers and fiber amplifiers. Optical Mater: X. 2023;17:100219. doi: 10.1016/j.omx.2022.100219

[116] Ma X, Liu L, Wu J. Nonlinear effects-based 1.7 μm fiber lasers: a review and prospect. MATEC Web Conf. 2023;382:01028. doi: 10.1051/matecconf/202338201028

[117] Soman SKO. A tutorial on fiber kerr nonlinearity effect and its compensation in optical communication systems. J Opt. 2021;23:123502. doi: 10.1088/2040-8986/ac362a

[118] Agrawal GP. Nonlinear fiber optics: its history and recent progress. J Opt Soc Am B. 2011;28:A1–10. doi: 10.1364/JOSAB.28.0000A1

[119] Schneider T. Nonlinear optics in telecommunications. Berlin, Heidelberg: Springer. 2013. doi: 10.1007/978-3-662-08996-5

[120] Bonetti J, Hernandez SM, Grosz DF. Master equation approach to propagation in nonlinear fibers. Opt Lett. 2021;46:665–668. doi: 10.1364/OL.417975

[121] Aso O, Tadakuma M, Namiki S. Four-wave mixing in optical fibers and its applications. dEp. 1999;1:2.

[122] Billington R. A report of four-wave mixing in optical fibre and its metrological applications. 1999.

[123] Sirleto L, Ferrara MA. Fiber amplifiers and fiber lasers based on stimulated Raman scattering: a review. Micromachines (Basel). 2020;11:247. doi: 10.3390/mi11030247

[124] Alexander VV, Kulkarni OP, Kumar M, et al. Modulation instability initiated high power all-fiber supercontinuum lasers and their applications. Optical Fiber Technol. 2012;18:349–374. doi: 10.1016/j.yofte.2012.07.014

[125] Xia C, Kumar M, Cheng M-Y, et al. Supercontinuum generation in silica fibers by amplified nanosecond laser diode pulses. IEEE J Select Top Quantum Electron. 2007;13:789–797. doi: 10.1109/JSTQE.2007.897414

[126] Kudlinski A, George AK, Knight JC, et al. Zero-dispersion wavelength decreasing photonic crystal fibers for ultraviolet-extended supercontinuum generation. Opt Express. 2006;14:5715–5722. doi: 10.1364/OE.14.005715

[127] Stone JM, Knight JC. Visibly "white" light generation in uniform photonic crystal fiber using a microchip laser. Opt Express. 2008;16:2670–2675. doi: 10.1364/OE.16.002670

[128] Conley NC, Choi SW, Buma T. Photoacoustic microscopy of lipids at 1.2 and 1.7 μm using a pulsed supercontinuum laser. 2017 IEEE International Ultrasonics Symposium (IUS). 06-09 September 2017 Washington, DC, USA. IEEE. 2017;1–4. doi: 10.1109/ULTSYM.2017.8092147

[129] Drexler W, Fujimoto JG. Optical Coherence Tomography. Berlin, Heidelberg: Springer. 2008. p. 1346. doi: 10.1007/978-3-540-77550-8

[130] Sun Y, Yang Q, Wang Y, et al. Extending laser wavelengths to 1630 nm in centimeter-scale Er-phosphate fiber. Opt Lett. 2023;48:456–459. doi: 10.1364/OL.480921

[131] Huang X, Huang X, Chen Z, et al. Near infrared luminescence properties and mechanism of high bismuth-doped SiO2-Al2O3-La2O3 glass. Opt Express. 2023;31:41783–41793. doi: 10.1364/OE.503498

[132] Raab M, Leaird D, Courtney TL, et al. Wavelength conversion through stimulated raman scattering in an oxygen-filled fiber for multi-band LiDAR. Opt Lett. 2024;49:1496–1499. doi: 10.1364/OL.513743